Indoor Localisation Uncertainty Control based on Wireless Ranging for Robots Path Planning

Farhad Shamsfakhr, Alessandro Antonucci, Luigi Palopoli, David Macii, *Senior Member, IEEE*, and Daniele Fontanelli, *Senior Member, IEEE*,

***Abstract*—The accurate localisation of robots in indoor environments is a well-known measurement problem, that becomes particularly critical in crowded scenarios, where the collision with obstacles, objects and human operators is very high. In this paper, the problem is solved through an optimal path planning strategy that keeps into account the ranging measurement uncertainty from a given set of wireless anchors (e.g., Ultra Wideband transceivers) that are used to track the position of the robot in a known reference frame through multilateration. In particular, assuming to use an Observability-based Filter (ObF), namely a position tracking estimator conceived to ensure the global observability of the robot state (namely its planar position and orientation) with quantifiable uncertainty, a potential-based path planning strategy is applied to drive the robot toward the goals while minimising the localisation uncertainty. Several simulation results using two alternative artificial potential functions confirm the correctness and the optimal performances of the proposed approach, which is entirely driven by observability and measurement uncertainty concerns and, as such, it is quite different and novel in the context of robots path planning techniques.**

***Keywords*—Indoor navigation, Path planning, Measurement uncertainty, Observability, Distance measurement.**

I. Introduction

In modern industrial practice, mobile robots are prominently used for moving goods between different areas of a factory. In crowded environments, especially when robots interact closely with human operators, a high level of robots autonomy is needed to decide the path towards the wanted destination. This scenario is technologically challenging and requires a high localisation accuracy all over the robot mission. In this paper, robot position and orientation are estimated through the fusion of dead reckoning and distance measurement data from a given set of wireless nodes (in the following referred to as "anchors" for brevity). Since position estimator performance strongly depends on the relative position of the robot and the anchors, a path planning technique minimising the localisation uncertainty in reaching the goal can be adopted [1]. The problem of robot localisation has received a constant attention over the last few years. In the wide range of technological options explored in the past, it is possible to mention fingerprinting of Wi-Fi signals [2], detection of radio frequency identification (RFID) tags [3], [4], computer vision techniques using both natural [5] and artificial landmarks [6], [7], and Light Detection and Ranging (LiDAR) sensors [8]. Particularly relevant to this paper are the multilateration solutions that exploit the distance of the robot from a set of wireless anchors with a known position in a given reference frame [9]. This distance can be estimated indirectly from the Received Signal Strength Indication (RSSI) values [10], [11] or through the Time-of-Arrival (ToA), the Time-Difference-of-Arrival (TDoA) or Round-Trip Time (RTT) measurement of the messages exchanged between each anchor and the wireless transceiver installed on the robot. In this respect, the use of Ultra-Wideband (UWB) signals [12] ensures a much higher accuracy (i.e., within a few cm) than the uncertainty achievable using RSSI or TDoA measurements from Wi-Fi devices, which is in the order of a few metres. The recent availability of new-generation, smaller and low-cost UWB transceivers (e.g., the DecaWave DW1000 [13]) has lowered the adoption barriers for this technology.

A key challenge arising from the use of anchor nodes is the need to reconcile high accuracy with low deployment and maintenance costs. In fact, the infrastructure has to be so sparse as possible, while ensuring that the system state (namely the planar position and orientation of the robot in the case at hand) is observable. The observability problem was analysed at a local level (i.e., when the initial state estimate is close enough to the actual one) in different papers [14], [15], [16]. In a previous work, we have studied the observability problem in a global sense in order to find the conditions for which the estimated states converge to the actual ones from any initial position [17]. Using this result, a position estimator ensuring global observability (and for this reason referred to as *Observability Filter* or ObF in the rest of this manuscript) and with the same performance of the Extended Kalman Filter (EKF) is described [18]. It is worth noticing that the ObF is less sensitive to a partial or wrong knowledge of the uncertainty affecting the adopted sensors [19].

The approach proposed in this paper is inspired by a previous work by Salaris et al. [20], in which the constructibility Gramian is used to locally mitigate the effect of uncertainties. This paper extends the content of [1] in three directions. Firstly, we have studied how to tune the parameter α that leverages the direction towards the goal with the growth of uncertainties. Secondly, the optimality of the proposed approach to find the path that leads to destination with the least uncertainty) is confirmed by Monte Carlo simulations. Finally, we have provided experimental evidence that the proposed approach can be easily and successfully implemented.

The paper is organised as follows: Section II describes

Farhad Shamsfakhr, David Macii and Daniele Fontanelli are with the Department of Industrial Engineering, Via Sommarive 5, 38123, Trento, Italy (e-mail: {farhad.shamsfakhr, david.macii, daniele.fontanelli}@unitn.it).

Alessandro Antonucci and Luigi Palopoli are with the Department of Information Engineering and Computer Science, University of Trento, Via Sommarive 9, 38123, Trento, Italy, (e-mail: luigi.palopoli@unitn.it).

the background and presents the problem. In Section III, we show how the closed-form expression of the uncertainty can be used in the context of a potential-based motion planning strategy. In Section IV we report several simulation results to substantiate our approach, to fine tune the parameter of the proposed solution and to show the optimality of the synthesised paths, while Section V offers experimental evidence of the applicability of the solution in an actual scenario. Finally, conclusions and future research directions are outlined in Section VI.

II. Background Material and Problem Formulation

In this section, after presenting the dynamic model of the robot, we quickly recall the definition of an observability filter for robot localisation based on a combination of on-board sensors and wireless devices able to measure the distance between the robot and a set of anchor nodes [19]. Then, we will set the background for the paper through a formal definition of the problem.

A. Models

Consider a unicycle robot moving across a space instrumented with m wireless anchor nodes (e.g., based on UWB signals), whose coordinates (X_i, Y_i) are known in a reference frame $\langle W \rangle$. Assuming that the sampling period of the ranging system is T_s, at each time step kT_s, $k \in \mathbb{N}$, the moving agent collects a set of distance measurement data. Such values are grouped together into the vector

$$z_k = \begin{bmatrix} z_{1,\,k} \\ z_{2,\,k} \\ \cdots \\ z_{m,\,k} \end{bmatrix} = \begin{bmatrix} \sqrt{(x_k - X_1)^2 + (y_k - Y_1)^2} \\ \sqrt{(x_k - X_2)^2 + (y_k - Y_2)^2} \\ \cdots \\ \sqrt{(x_k - X_m)^2 + (y_k - Y_m)^2} \end{bmatrix}, \tag{1}$$

where (x_k, y_k) are the Cartesian coordinates of the mid-point of the unicycle wheel axle. Under the customary assumption that the forward v_k and angular ω_k velocities of the vehicle are held constant during each sampling interval $[kT_s, (k+1)T_s]$, it is possible to find the following discrete–time equivalent dynamics for the robot [17], i.e.

$$\begin{aligned} x_{k+1} &= x_k + \Phi_k \cos(\theta_k) - \Psi_k \sin(\theta_k) = x_k + \delta_{x_k}, \\ y_{k+1} &= y_k + \Psi_k \cos(\theta_k) + \Phi_k \sin(\theta_k) = y_k + \delta_{y_k}, \\ \theta_{k+1} &= \theta_k + 2\phi_k, \end{aligned} \tag{2}$$

where

$$\phi_k = \frac{\omega_k}{2} T_s \text{ and } A_k = 2\frac{v_k}{\omega_k} \sin\left(\frac{\omega_k}{2} T_s\right), \tag{3}$$

$\Phi_k = A_k \cos(\phi_k)$ and $\Psi_k = A_k \sin(\phi_k)$. We will exploit the fact that when $\omega_k \to 0$, the A_k coefficient takes its limit value:

$$\lim_{\omega_k \to 0} A_k = \lim_{\omega_k \to 0} 2\frac{v_k}{\omega_k} \sin\left(\frac{\omega_k}{2} T_s\right) = v_k T_s.$$

For the sake of clarity, Fig. 1 shows the most relevant quantities of model describing robot dynamics.

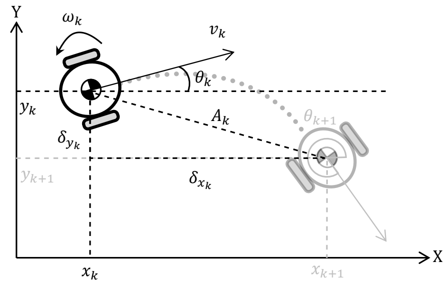

Fig. 1. Graphical qualitative representation of the main quantities of interest of the discrete-time system model based on equations (2) and (3).

B. Observability

As stated in [17], the use of $m \geq 3$ non-collinear anchor nodes avoids any ambiguity in estimating any trajectory with $v_k \neq 0$, thus enabling global observability if trilateration or multilateration from the anchors is applied twice in a row when the robot moves between two different nearby positions. Indeed, as known, the Cartesian coordinates (x_k, y_k) of the robot as well as its initial position can be determined from at least three distance values. In particular, given

$$\begin{aligned} z_{i,k}^2 &= (x_k - X_i)^2 + (y_k - Y_i)^2 = \\ &= X_i^2 + x_k^2 + y_k^2 + Y_i^2 - 2X_i x_k - 2Y_i y_k, \end{aligned} \tag{4}$$

with $i = 1, \ldots, m$, by subtracting $z_{i,k}^2$ from $z_{1,k}^2$, i.e. $\Delta_{i,k} = z_{1,k}^2 - z_{i,k}^2$, we get

$$h_k^{(m)} = 2\Sigma^{(m)} \begin{bmatrix} x_k \\ y_k \end{bmatrix} = \begin{bmatrix} \Delta_{2,k} - X_1^2 - Y_1^2 + X_2^2 + Y_2^2 \\ \Delta_{3,k} - X_1^2 - Y_1^2 + X_3^2 + Y_3^2 \\ \vdots \\ \Delta_{m,k} - X_1^2 - Y_1^2 + X_m^2 + Y_m^2 \end{bmatrix}, \tag{5}$$

where

$$\Sigma^{(m)} = \begin{bmatrix} X_2 - X_1 & Y_2 - Y_1 \\ X_3 - X_1 & Y_3 - Y_1 \\ \vdots & \vdots \\ X_m - X_1 & Y_m - Y_1 \end{bmatrix}. \tag{6}$$

Observe that using three non-collinear anchors (5), matrix $\Sigma^{(3)}$ is invertible and the planar position (x_k, y_k) can be estimated bu reversing (5). Also, the orientation angle θ_k can be estimated indirectly from (2) once the coordinates of the robot (x_k, y_k) and (x_{k+1}, y_{k+1}) in two consecutive positions are known. In particular, if $R(\phi_k)$ denotes the two-dimensional rotation matrix of angle ϕ_k, we have that

$$A_k R(\phi_k) \begin{bmatrix} \cos(\theta_k) \\ \sin(\theta_k) \end{bmatrix} = \begin{bmatrix} x_{k+1} - x_k \\ y_{k+1} - y_k \end{bmatrix}, \tag{7}$$

which finally returns $\theta_k = \arctan\left(\frac{\sin(\theta_k)}{\cos(\theta_k)}\right)$.

C. Observability filter design

Using the global observability analysis described in Section II-B, it is possible to design an ObF for a number of anchors $m \geq 3$, as explained in [19]. In particular, the planar coordinates of the robot are given by the Weighted Least Squares (WLS) solution

$$\begin{bmatrix} \hat{x}_k \\ \hat{y}_k \end{bmatrix} = \frac{1}{2} (\Sigma^{(m)^T} N_k^{(m)^{-1}} \Sigma^{(m)})^{-1} \Sigma^{(m)^T} N_k^{(m)^{-1}} h_k^{(m)}. \quad (8)$$

where the estimation errors $\widetilde{x}_k = \hat{x}_k - x_k$ and $\widetilde{y}_k = \hat{y}_k - y_k$ are grouped in the position estimation error vector $\xi_k = [\widetilde{x}_k, \widetilde{y}_k]^T$, whose covariance matrix is

$$\Xi_k^{(m)} = (\Sigma^{(m)^T} N_k^{(m)^{-1}} \Sigma^{(m)})^{-1} = \begin{bmatrix} \sigma_{x,k}^2 & \sigma_{xy,k} \\ \sigma_{xy,k} & \sigma_{y,k}^2 \end{bmatrix}, \quad (9)$$

and the weighting matrix is

$$N_k^{(m)} = \sigma_\rho^2 \begin{bmatrix} z_{1,k}^2 + z_{2,k}^2 & z_{1,k}^2 & \cdots & z_{1,k}^2 \\ z_{1,k}^2 & z_{1,k}^2 + z_{3,k}^2 & \cdots & z_{1,k}^2 \\ \vdots & & \ddots & \vdots \\ z_{1,k}^2 & z_{1,k}^2 & \cdots & z_{1,k}^2 + z_{m,k}^2 \end{bmatrix}. \quad (10)$$

In (10), terms $\tilde{z}_{i,k}$ are assumed to be Gaussian, white and zero-mean noises with variance σ_ρ^2. As a result, the closed-form expressions of the elements of (9) can be obtained [19]. As far as robot orientation estimation is considered instead, we have that

$$\hat{\theta}_k = \arctan \left(\frac{\cos(\overline{\phi}_k)(\hat{y}_{k+1} - \hat{y}_k) - \sin(\overline{\phi}_k)(\hat{x}_{k+1} - \hat{x}_k)}{\sin(\overline{\phi}_k)(\hat{y}_{k+1} - \hat{y}_k) + \cos(\overline{\phi}_k)(\hat{x}_{k+1} - \hat{x}_k)} \right), \quad (11)$$

that approximated to the first order gives $\hat{\theta}_k \approx \theta_k + \widetilde{\theta}_k$ with variance

$$\sigma_{\theta_k}^2 = \frac{\sigma_\omega^2 T_s^2}{4} + \frac{1}{A_k^4} B_k (\Xi_k^{(m)} + \Xi_{k+1}^{(m)}) B_k^T, \quad (12)$$

where $B_k = [\delta_{y_k}, -\delta_{x_k}]$, $\delta_{x_k} = x_{k+1} - x_k$, $\delta_{y_k} = y_{k+1} - y_k$, $A_k^2 = \delta_{x_k}^2 + \delta_{y_k}^2$ and Ξ_k is reported in (9). Of course, to design a dynamic estimator the orientation angle estimate at the same time instant of the last collected measurement, i.e. at $(k+1)T_s$ is needed. Therefore, the vehicle dynamic (2) can be used (even if it is affected by uncertainty) to propagate the angle estimate one step forward. As a result, the uncertainty contributions $\widetilde{\theta}_{k+1} = \widetilde{\theta}_k + \eta_k T_s$ affecting $\hat{\theta}_{k+1}$ also exhibit zero mean and variance $\sigma_{\theta_{k+1}}^2 = \sigma_{\theta_k}^2 + T_s^2 \sigma_\omega^2$. Finally, the estimated state $\hat{s}_{k+1} = [\hat{x}_{k+1}, \hat{y}_{k+1}, \hat{\theta}_{k+1}]^T$ is affected by an uncertainty contribution $[\xi_{k+1}^T, \widetilde{\theta}_{k+1}]^T$, whose covariance matrix is

$$\Gamma_{k+1} = \begin{bmatrix} \Xi_{k+1}^{(m)} & \Xi_{k+1}^{(m)} B_{k+1}^T \\ B_{k+1} \Xi_{k+1}^{(m)} & \sigma_{\theta_{k+1}}^2 \end{bmatrix}. \quad (13)$$

III. Minimising uncertainty through robot path planning

In this section, the path planning technique used to reach a final destination while minimising the localisation uncertainty is described. Specifically, a planning solution based on Artificial Potential Fields (APF) is adopted [21]. The idea is to compute a balanced composition between two different potential fields. Function $V_{goal}(x, y) = [(x - X_{goal})^2 + (y - Y_{goal})^2]$ defines a potential function having a minimum on the target position; hence, its gradient is directed towards the desired location. Function $\tilde{V}(x, y)$, instead, has a minimum in the position of the motion plane with minimum uncertainty, therefore its gradient directed towards the locations that minimise position uncertainties. The overall resulting potential field is then given by

$$V_{tot}(x, y) = \alpha V_{goal}(x, y) + \tilde{V}(x, y). \quad (14)$$

The parameter $\alpha > 0$ is a tuning factor ruling the balance between attraction towards the desired goal position (which increases as α grows) and the localisation uncertainty. Clearly, the direction of motion of the robot is point-wise given by the weighted sum (by means of α) of the gradients of the two potential fields, i.e., the gradient of $V_{tot}(x, y)$. At each time step k, the robot navigation algorithm:

1) Estimates the robot position $(\hat{x}_k, \hat{y}_k)$ and the orientation θ_k;
2) Computes the gradient $\nabla_{x_k, y_k} V_{tot}(\hat{x}_k, \hat{y}_k)$;
3) Sets the model inputs of the robot position in (2) as $\delta_{x_k} = \gamma u_{1,k}$ and $\delta_{y_k} = \gamma u_{w,k}$, where $\mathbf{u}_k = [u_{1,k}, u_{2,k}]^T$ is the unit vector of the gradient direction $\nabla_{x_k, y_k} V_{tot}(\hat{x}_k, \hat{y}_k)$, and γ is the magnitude of the input determined by the orientation uncertainties, as explained in the next Section;
4) Determines the robot linear and angular velocities v_k and ω_k by using (2) and inverting
$$\gamma \mathbf{u}_k = \begin{bmatrix} \delta_{x_k} \\ \delta_{y_k} \end{bmatrix} = \begin{bmatrix} \Phi_k \cos(\theta_k) - \Psi_k \sin(\theta_k) \\ \Psi_k \cos(\theta_k) + \Phi_k \sin(\theta_k) \end{bmatrix}.$$
Moreover, using (3) after some algebraic steps it results that
$$\omega_k = \frac{2 \arctan\left(\frac{b}{a}\right)}{T_s} \text{ and } v_k = \frac{\gamma^2 \arctan\left(\frac{b}{a}\right)}{b T_s},$$
where $a = \cos(\theta_k)\delta_{x_k} + \sin(\theta_k)\delta_{y_k}$ and $b = -\sin(\theta_k)\delta_{x_k} + \cos(\theta_k)\delta_{y_k}$. Notice that when $\omega_k \approx 0$, we have $v_k = \frac{\gamma}{T_s}$.
Thus, some possible input constraints can be taken into account for feasible maximum values of v_k and ω_k.

The overall algorithm is depicted in Figure 2. Two different APF solutions are reported in the rest of the section.

A. ObF-based potential field

In the first APF synthesis, the localisation uncertainty is given by the trace of the matrix Γ_{k+1} in (13) considering only the position related quantities. The term $\tilde{V}(x, y)$ in (14) is then given by $\text{Tr}\left(\Xi_k^{(m)}\right)$, which in turn results from

$$\text{Tr}\left(\Xi_k^{(m)}\right) = \text{Tr}\left((\Sigma^{(m)^T} N_k^{(m)^{-1}} \Sigma^{(m)})^{-1}\right) \propto \text{Tr}\left(N_k^{(m)}\right), \quad (15)$$

Since the variance of the the estimated robot position is directly proportional to the distance measurements from the anchors, it follows from (10) that

$$\text{Tr}\left(N_k^{(m)}\right) = \sigma_\rho^2 \left[(m-1) z_{1,k}^2 + \sum_{i=2}^{m} z_{i,k}^2\right]. \quad (16)$$

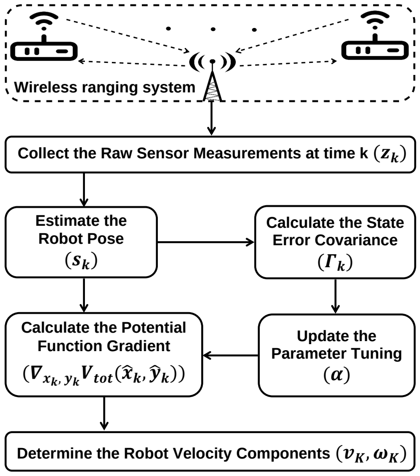

Fig. 2. Overview of the proposed path planning algorithm.

Therefore, the gradient of the trace function becomes

$$\frac{\partial \mathrm{Tr}\left(N_k^{(m)}\right)}{\partial x_k} = 2\left[(m-1)(x_k - X_1) + \sum_{i=2}^{m}(x_k - X_i)\right]$$
$$\frac{\partial \mathrm{Tr}\left(N_k^{(m)}\right)}{\partial y_k} = 2\left[(m-1)(y_k - Y_1) + \sum_{i=2}^{m}(y_k - Y_i)\right]. \tag{17}$$

Hence the direction of the gradient of the potential function (14) is given by:

$$\nabla_{x_k,\, y_k} V_{tot} = \begin{bmatrix} 2\left((m-1)(x_k - X_1) + \sum_{i=2}^{m}(x_k - X_i)\right) + 2\alpha(x_k - X_{goal}) \\ 2\left((m-1)(y_k - Y_1) + \sum_{i=2}^{m}(y_k - Y_i)\right) + 2\alpha(y_k - Y_{goal}) \end{bmatrix}^T \tag{18}$$

As far as the variance $\sigma^2_{\theta_{k+1}}$ of the estimated angle is concerned, given two consecutive measurements at times k and $k+1$, respectively, it follows from (12) that

$$\sigma^2_{\theta_{k+1}} = \frac{5\sigma_\omega^2 T_s^2}{4} + \frac{1}{A_k^4} B_k(\Xi_k^{(m)} + \Xi_{k+1}^{(m)})B_k^T, \tag{19}$$

where the first term on the rightmost side of (19) is constant and the second one is the directly related to the input values. Observing that the relation between the values of (9) in two consecutive time instants k and $k+1$ can be obtained by combining (4) and (2), it results that

$$\begin{aligned} z^2_{i,\,k+1} &= z^2_{i,\,k} + A_k^2 + 2\left[\delta_{x_k}(x_k - X_i) + \delta_{y_k}(y_k - Y_i)\right] = \\ &= z^2_{i,k} + A_k^2 + \Delta z_{i,k}, \end{aligned} \tag{20}$$

where it is explicitly shown that the change of range is proportional to the projection of the displacement of the robot along the line joining the robot position and the anchor position at time k, i.e.

$$\Delta z_{i,k} = 2\left\langle \begin{bmatrix} x_k - X_i \\ y_k - Y_i \end{bmatrix}, \begin{bmatrix} \delta_{x_k} \\ \delta_{y_k} \end{bmatrix} \right\rangle. \tag{21}$$

Recalling that $A_k^2 = \delta^2_{x_k} + \delta^2_{y_k}$, it is then possible to plug (20) into (9) and retrieve a nice dependence of $\Xi_{k+1}^{(m)}$ on $\Xi_k^{(m)}$, δ_{x_k} and δ_{y_k}. Since $[\delta_{x_k}, \delta_{y_k}]^T = \gamma \mathbf{u}_k$, the uncertainty $\sigma^2_{\theta_{k+1}}$ becomes a function of γ. Indeed, by defining

$$\Theta(\Xi_k^{(m)}, \gamma \mathbf{u}_k) = \Xi_k^{(m)} + \Xi_{k+1}^{(m)} = \begin{bmatrix} \underline{\sigma}^2_{x,k+1} & \underline{\sigma}_{xy,k+1} \\ \underline{\sigma}_{xy,k+1} & \underline{\sigma}^2_{y,k+1} \end{bmatrix}, \tag{22}$$

where $\underline{\sigma}^2_{x,k+1} = \sigma^2_{x,k+1} + \sigma^2_{x,k}$, $\underline{\sigma}^2_{y,k+1} = \sigma^2_{y,k+1} + \sigma^2_{y,k}$ and $\underline{\sigma}_{xy,k+1} = \sigma_{xy,k+1} + \sigma_{xy,k}$, we finally have that $\sigma^2_{\theta_{k+1}}(\gamma)$. Therefore, if a gradient-based descent approach is adopted, it follows that $\gamma = \operatorname{argmin} \sigma^2_{\theta_{k+1}}(\gamma)$.

B. GDOP-based potential field

For the sake of comparison, instead of minimising the trace of $N_{k+1}^{(m)}$, the minimisation of the Geometric Dilution of Precision (GDOP) is considered as an alternative strategy. This approach is inspired to the Global Positioning Systems (GPS) problems and expresses the ranging-based position estimation uncertainties considering only the geometry of the anchors deployment [22]. In the following, to refer to either method, acronyms TM (Trace minimisation) and GM (GDOP minimisation) will be used in the former and in the latter case, respectively. If H_k denotes the Jacobian of (1), its i-th row is given by

$$H_{i,k} = \begin{bmatrix} \frac{x_k - X_i}{z_{i,k}} & \frac{y_k - Y_i}{z_{i,k}} \end{bmatrix} = \begin{bmatrix} \cos(\eta_i) & \sin(\eta_i) \end{bmatrix}, \tag{23}$$

where $\eta_i = \arctan(\frac{y_k - Y_i}{x_k - X_i})$. Also, the best linear unbiased estimator (BLUE) of the target position has the following covariance matrix $\Xi_k^{(m)} = (H_k^T R^{-1} H_k)^{-1} = \frac{1}{\sigma_\rho^2}(H_k^T H_k)^{-1}$, in which $R = \sigma_\rho^2 I_m$ is the covariance of the distance measurements and I_m is the identity matrix of order m. Since the GDOP depends only on geometric features and not on the actual ranging uncertainty contributions [22], it is implicitly assumed that $\sigma_\rho^2 = 1$, which yields the potential function $\tilde{V}(x_k, y_k) = \sqrt{\mathrm{Tr}\left(H_k^T H_k^{-1}\right)}$. To compute the gradient of this potential function, we first notice that

$$H_k^T H_k = \begin{bmatrix} \sum_{i=1}^{m} \cos(\eta_i)^2 & \sum_{i=1}^{m} \cos(\eta_i)\sin(\eta_i) \\ \sum_{i=1}^{m} \cos(\eta_i)\sin(\eta_i) & \sum_{i=1}^{m} \sin(\eta_i)^2 \end{bmatrix} \tag{24}$$

and, then, through simple algebraic manipulations, it follows that

$$\tilde{V}(x_k, y_k) = \sqrt{\frac{m}{\sum_{i=1}^{m-1}\sum_{j=i+1}^{m} \sin^2(\eta_i - \eta_j)}} = \sqrt{\frac{m}{\beta}}. \tag{25}$$

If we define $\delta_{\eta_{i,j}} = \eta_i - \eta_j$, it finally results that

$$\frac{\partial \tilde{V}(x_k, y_k)}{\partial x_k} = -\frac{\sqrt{m}}{\beta\sqrt{\beta}} \Bigg[\sum_{i=1}^{m-1} \sum_{j=i+1}^{m} \sin(\delta_{\eta_{i,j}}) \cos(\delta_{\eta_{i,j}}) + \frac{y_k - Y_i}{z_{i,k}^2} - \frac{y_k - Y_j}{z_{j,k}^2} \Bigg],$$

$$\frac{\partial \tilde{V}(x_k, y_k)}{\partial y_k} = -\frac{\sqrt{m}}{\beta\sqrt{\beta}} \Bigg[\sum_{i=1}^{m-1} \sum_{j=i+1}^{m} \sin(\delta_{\eta_{i,j}}) \cos(\delta_{\eta_{i,j}}) + \frac{x_k - X_i}{z_{i,k}^2} - \frac{x_k - X_j}{z_{j,k}^2} \Bigg]. \tag{26}$$

We can therefore plug (26) into (18) and then proceed as described. Instead, for the orientation it is sufficient to use (22) substituting the corresponding covariance matrices $\Xi_k^{(m)}$ and $\Xi_{k+1}^{(m)}$ with the GDOP related matrices $\overline{\Xi}_k^{(m)}$ and $\overline{\Xi}_{k+1}^{(m)}$.

IV. Simulation Results

The performance of the proposed approach is investigated through extensive simulations. We first provide an analysis to choose between the TM and the GM approach. Then, an empirical sensitivity analysis to tune parameter α in (14) is reported. Finally, the solutions obtained with the unicycle robot moving along the respective optimal paths are compared in terms of both efficiency in reaching the goal and localisation uncertainty growth. In all the simulations, both the wheel encoders data and the UWB distance measurements from the anchors are assumed to be collected and processed with a sampling period of $T_s = 100$ ms.

A. TM vs. GM comparison

Initially, $\alpha = 30$ in (14) to ensure convergence towards the goal. The uncertainty contributions of robot linear and angular velocities v_k and ω_k due to encoders are assumed to be white and normally distributed, with zero-mean and standard deviations $\sigma_v \in [0.001, 0.2]$ m/s and $\sigma_\omega \in [0.001, 0.2]$ rad/s, respectively. The UWB distance measurements are affected by normally distributed, zero-mean and white uncertainty contributions with standard deviations included in the interval $\sigma_\rho \in [0.01, 0.1]$ m. The values of $\tilde{V}(x_k, y_k)$ for GM and TM optimisation depicted in Fig. 3 assuming that $m = 3$ UWB anchors are deployed in two different ways. The expression of $\mathrm{Tr}\left(N_k^{(m)}\right)$ in the TM case returns a smooth paraboloid regardless of anchor position (Figure 3-a,b), wheres the GDOP function yields a complicated error surface (Figure 3-c,d).

A qualitative analysis of the trajectories obtained with the described approach in the cases depicted in Fig. 3-b,d, is shown in Fig. 4. In this example, the initial state of the robot is $s_i = [2\text{ m}, 8\text{ m}, 0\text{ rad}]$, while the final position is $s_e = [12\text{ m}, 10\text{ m}]$. It is worth noticing that the final orientations of the paths obtained with the TM and the GM methods are different (i.e., 0.7 rad in the former case and -2.79 rad in the latter) because the final position is reached following different paths.

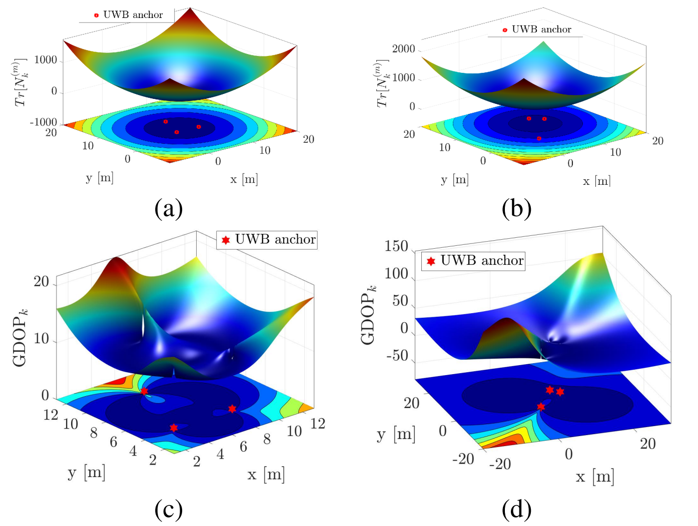

Fig. 3. Representation of the $\tilde{V}(x_k, y_k)$ for TM (a,b) and GM (c,d) optimisations calculated over the entire simulation area. Two different deployment of $m = 3$ UWB anchors are adopted in (a,c) and (b,d), respectively.

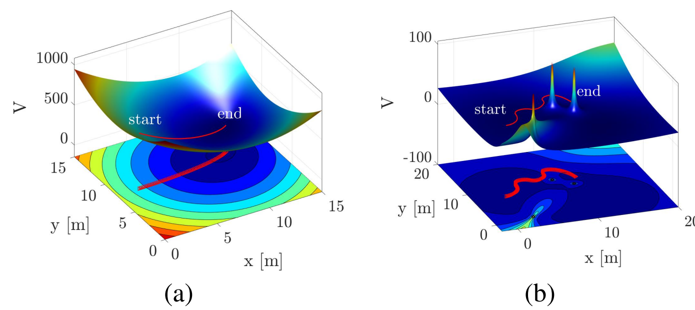

Fig. 4. Sample controlled trajectories for the TM (a) and the GM (b) in the scenarios depicted in Figure 3-b,d.

For a quantitative comparison, a Monte Carlo (MC) analysis over 15000 runs (i.e. 1000 paths in 15 different conditions of sensor noises) was performed, assuming that the initial and final positions of the robots are the same as before. For the sake of brevity, only the results with the anchors placed, as shown in Figure 3-b,d are reported. In particular, the Root Mean Square (RMS) localisation errors (i.e., the square root of the mean of $\|\xi_k\|$) and the RMS of the orientation angle) are plotted in Figure 5-a,b. It can be noticed that the GM yields better results in orientation, but a larger positioning RMS error. Another important result of the analysis is that as the uncertainties grow, the difference between the two approaches becomes minor. In general, we can conclude that the TM is preferable to the GM approach, since the potential function to optimise in the former case exhibits a simple paraboloid shape (as shown in Figure 3), which makes optimisation simpler.

B. α parameter tuning

To determine the optimal value of α in the TM case, a further MC analysis is performed. In all the simulated scenarios, two alternative sets of anchors positions (i.e., symmetric

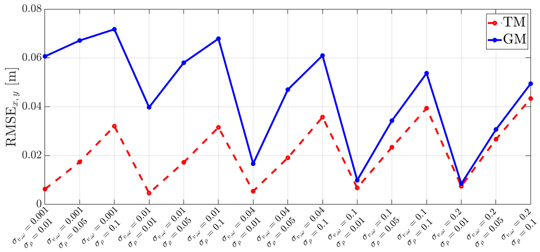

(a)

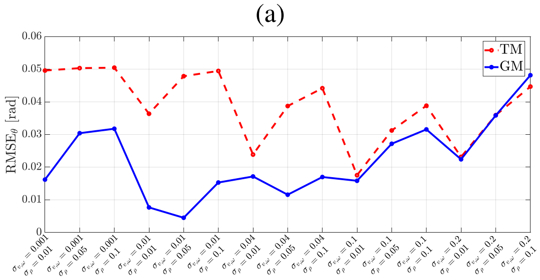

(b)

Fig. 5. Position (a) and orientation (b) RMSE for the TM (dashed) and the GM (solid) approaches with different velocity uncertainties (we assume $\sigma_{v\omega} = \sigma_v = \sigma_\omega$) and different ranging uncertainties σ_ρ with the anchors placed as shown in Figure 3-b,d.

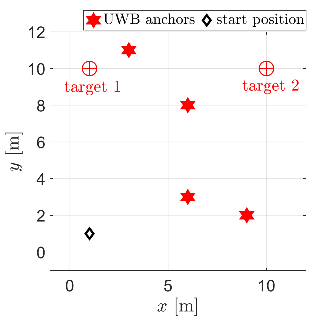

(a)

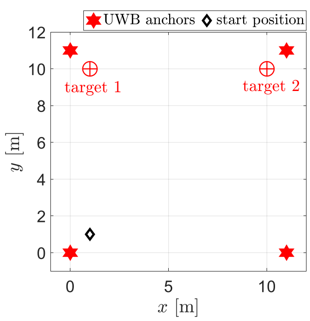

(b)

Fig. 6. The environment used for α tuning, with (a) asymmetric and (b) symmetric anchor positions.

and non-symmetric) and two different target locations are considered, as shown in Figure 6. The maximum value for reaching the target was limited to 14 seconds (70 time steps).

As a cost function, the minimum localisation uncertainty (regardless of the anchors location and the destination point) is considered while ensuring final position reachability. Notice that this is a very challenging problem since there are many parameters to be considered (anchor deployment and target location), and it is further complicated by the fact that in general α should not be constant. Indeed, driving the robot towards its final state when the localisation uncertainty is too high is useless. This suggests the value of α should be small. On the other hand, keeping the value of α too small may prevent convergence towards the goal. To this end, two different functions for the tuning factor are considered. First, we express α as follows

$$\alpha(t) = \varphi(1+\tau)^t, \tag{27}$$

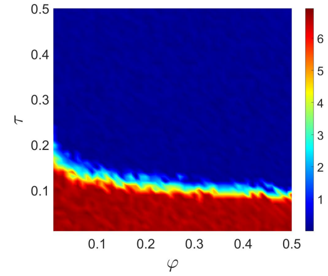

(a)

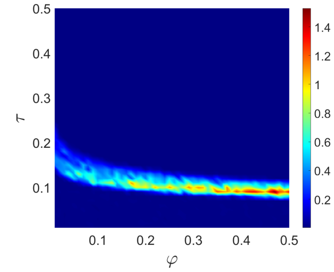

(b)

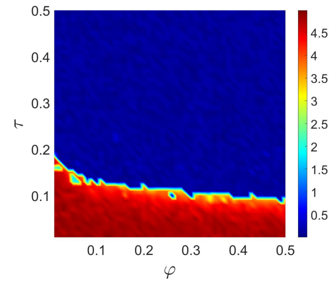

(c)

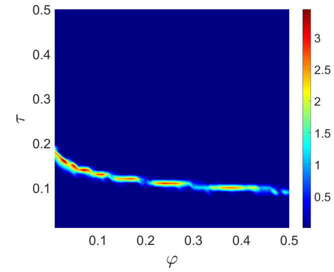

(d)

Fig. 7. MC results for the target destination labelled as 1 in Figure 6. Average and target distance error at the end of the simulated path using the symmetric (a) and asymmetric (c) anchor deployment. The respective variances are plotted in (b) and (d). The right-hand side colour bars are expressed in m and m^2, respectively.

where $\varphi > 0$ accounts for the initial value of α at time $t = 0$ and $\tau > 0$ takes into account the rate of growth of α over time. For instance, by choosing very small values of τ (e.g. $\tau \leq 0.001$) we have that α is approximately a linear function of time.

In the first scenario shown in Figure 6, 500 tests were simulated. In each test, 2500 possible robot paths were synthesised for 2500 different values of parameters $\varphi = [0.01, \dots, 0.5]$ and $\tau = [0.01, \dots. 0.5]$ resulting in 1250000 different trajectories. Then, for each pair of values (φ, τ), the average and the variance of the distance between the last point of the simulated path and each target destination point were computed. In all tests, Gaussian and uncorrelated random noises with zero mean and standard deviations $\sigma_\rho = 0.3$ m, $\sigma_v = 0.1$ m/s and $\sigma_w = 0.06$ rad/s were used. The average and variance values obtained with the symmetric and asymmetric anchor deployments for either one of the target destination points shown in Figure 6 are depicted as a function of φ and τ in Figure 7-a,d and Figure 8-a,d, respectively. As can be seen in the graphs, with $\varphi \geq 0.1$ and $\tau \geq 0.15$ the destination can be reached with standard uncertainty of about 1 m.

We used those values to evaluate the localisation uncertainty along the paths. In particular, we used 16 different values of $\varphi \geq 0.1$ and $\tau \geq\geq 0.1$ using two different uncertainty conditions, which are called *medium*, (with $\sigma_\rho = 0.3$ m, $\sigma_v = 0.1$ m/s and $\sigma_w = 0.06$ rad/s) and *high* (with $\sigma_\rho = 0.5$ m, $\sigma_v = 0.2$ m/s and $\sigma_w = 0.1$ rad/s). Again, both the symmetric and the asymmetric deployments of the anchor nodes are considered. The graphs of Figure 9, reporting the standard deviation of the estimated position (Figure 9-a,c) and of the

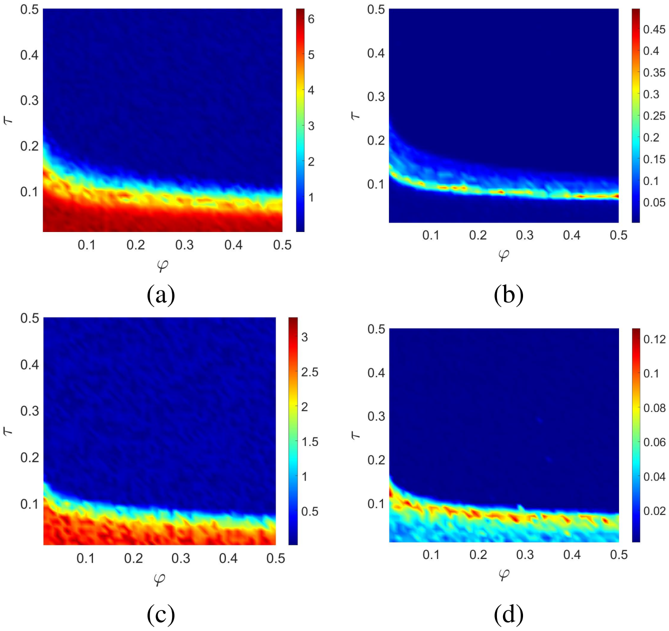

Fig. 8. MC results for the target destination labelled as 2 in Figure 6. Average and target distance error at the end of the simulated path using the symmetric (a) and asymmetric (c) anchor deployment. The respective variances are plotted in (b) and (d). The right-hand side colour bars are expressed in m and m^2, respectively.

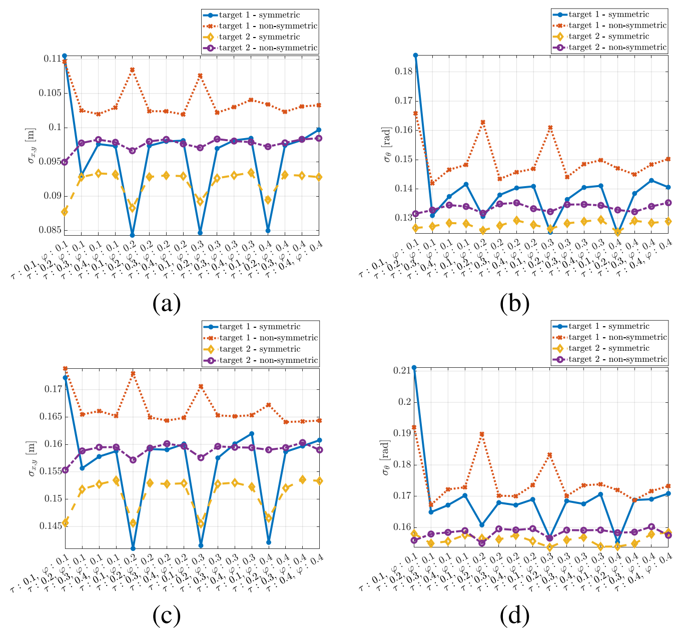

Fig. 9. Localisation standard uncertainties for different values of the parameters of (27) in the presence of medium (a, b) and high (c, d) measurement noise conditions.

estimated orientation, respectively, (Figure 9-b,d), clearly show that the same values of the exponential tuning factor α can have a completely different impact on performances. This behaviour is due to the first-order linearisation in the computation of the trace in (13) as well as to the specific anchor geometry. For this reason, if α is computed through (27), results are not univocal.

To solve this problem, additional tests have been carried out considering

$$\alpha = \zeta \mathrm{Tr}\left(\Gamma_{k+1}^{-1}\right), \tag{28}$$

where $\zeta > 0$ is a single tuning parameter. The main idea is that, the more the uncertainty decreases, the more the robot is attracted towards the final destination. If the distributions of the errors at the target destination points are plotted as a function of ζ (see the box-and-whiskers plots in Figure 10-a,d), it turns out that for $\zeta \geq 0.05$ an average target error lower than 1 m can be achieved. Thus, this range of values can be chosen to evaluate the standard uncertainties associated with planar position and orientation estimation in the medium and high sensor uncertainty conditions mentioned above (see Figure 11-a,d). This time, the results are consistent and the benefit of increasing ζ is more evident with high uncertainties (see Figure 11-c,d). This result once more highlights the importance of the uncertainty for the control of mobile robots.

C. Path optimality

In this section we investigate the optimality of the trajectories obtained with the TM approach. To carry out this test, the optimal trajectories to reach the target destination points in Figure 6 are synthesised with an alternative method, which takes into account the final distance to the target, the total time to accomplish the goal and the maximum robot localisation uncertainty. To solve this challenging problem, we used 400000 MC randomly generated trajectories from the initial position $s_i = [1, 1]$ m to the target locations using both the symmetric and asymmetric deployments of the anchor nodes (see Figure 6). In this case, the standard deviation values of the sensor noises are set to $\sigma_\rho = 0.5$ [m], $\sigma_v = 0.1$ [m/s] and $\sigma_\omega = 0.06$ [rad/s]. Since we are interested in a multi-objective optimal path (taking into account the distance, the time and the uncertainty, as mentioned above), we first discretised the path (comprising a sequence of x_k, y_k and θ_k as in (2)) on a three-dimensional grid with $\Lambda_x = \{\lambda_{x,1}, \dots, \lambda_{x,10}\}$ and $\lambda_{x,i} = i$ [m] (i.e, with resolution of 1 m), $\Lambda_y = \Lambda_x$ and $\Lambda_\theta = \{\lambda_{\theta,0}, \lambda_{\theta,0.034}, \dots, \lambda_{\theta,2\pi}\}$ rad (i.e., with resolution of 0.034 [rad]). We assume that a point $[x_k, y_k, \theta_k]$ of the path passes through the grid point $[\lambda_{x,i}, \lambda_{y,j}, \lambda_{\theta,q}]$ if

$$\Pr \left\| \begin{bmatrix} x_k \\ y_k \\ \theta_k \end{bmatrix} - \begin{bmatrix} \lambda_{x,i} \\ \lambda_{y,j} \\ \lambda_{\theta,q} \end{bmatrix} \right\| \geq 0.95.$$

More in depth, assume that the localisation uncertainty covariance matrix is estimated with an EKF along the trajectories, hence the previous probability can be easily computed considering that the pdf of the uncertainties is implicitly defined as a Gaussian, here considered as a likelihood function. Notice that, since s_i and s_e lies on two grid points, each path has at the very least two grid points.

Next, to account for the uncertainty, we considered that each grid element is extended with extended with σ_x, σ_y and σ_ω, i.e., the standard deviations on the diagonal of

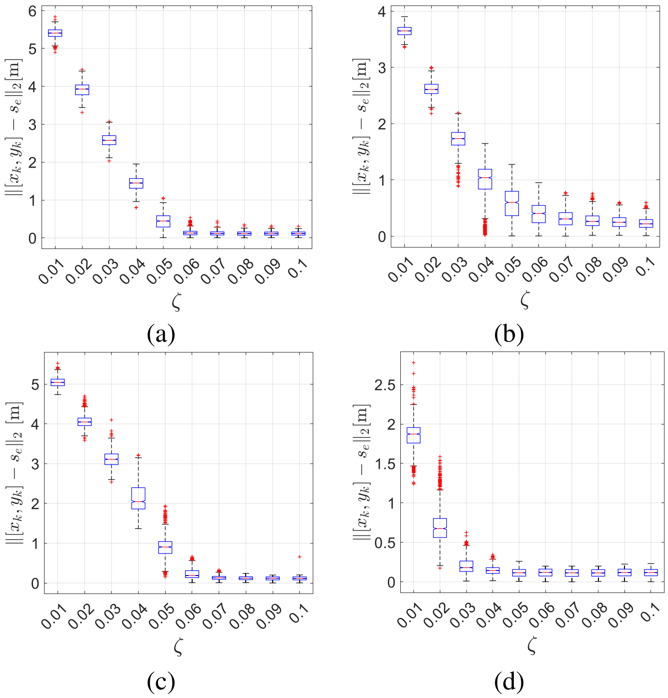

Fig. 10. Average distance errors from the target destination points 1 (a,b) and 2 (c,d) when the symmetric (a,c) and asymmetric (b,d) deployments of the anchors shown in Figure 6 are used.

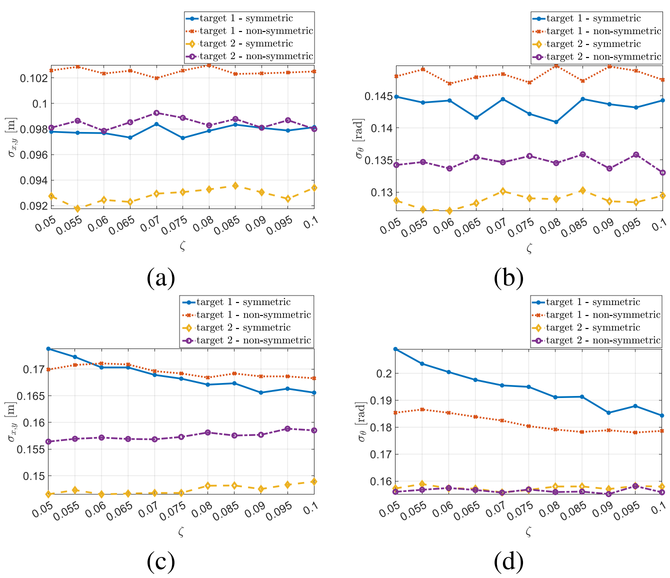

Fig. 11. Localisation standard uncertainties for the different values of the parameters of (28) in the presence of medium (a, b) and high (c, d) measurement noise conditions.

the localisation error covariance matrix estimated with the EKF previously mentioned, thus obtaining a six-dimensional grid point. Using the histograms of the MC simulations, the grid choice for these additional three components was set to $\Lambda_{\sigma_x} = \{6, \ldots, 126\}$ mm (i.e, with resolution of 6 [mm]), $\Lambda_{\sigma_y} = \Lambda_{\sigma_x}$ and $\Lambda_{\sigma_\theta} = \{5, \ldots, 100\}$ [mrad] (i.e, with resolution of 5 [mrad]).

	Target	Anchors deployment	$\lceil P_x \rceil$	$\lceil P_y \rceil$	$\lceil P_\theta \rceil$
Graph	[1, 10]	symmetric	0.013	0.011	0.007
	[10, 10]	symmetric	0.012	0.011	0.005
	[1, 10]	asymmetric	0.015	0.013	0.007
	[10, 10]	asymmetric	0.013	0.013	0.007
APF	[1, 10]	symmetric	0.018	0.017	0.010
	[10, 10]	symmetric	0.018	0.017	0.009
	[1, 10]	asymmetric	0.019	0.020	0.009
	[10, 10]	asymmetric	0.019	0.020	0.010

TABLE I. THE COMPARISON BETWEEN THE OPTIMAL GRAPH-BASED SOLUTION AND THE PROPOSED APF-BASED SOLUTION.

By arranging the grid points as nodes of a graph (we obtained by the MC simulated trials 600000 unique nodes) and assuming that two nodes are connected if there exists a path (or a portion of a path) connecting them, each edge is weighted by the sum of the maximum of the trace of the EKF uncertainty covariance matrix along all the paths connecting the two nodes and the maximum of the number of time steps taken to connect one node to another. It is then possible to compute the optimal path by executing the Bellman-Ford algorithm on the weighted thus derived graph. The inputs to the Bellman-Ford algorithm are the start s_i and target s_e positions, and its outputs are the maximum trace of the EKF between the starting and ending positions and the total elapsed time (regarded as the maximum time limit for our method). For the sake of comparison, our solution is tested over 10000 MC runs in order to have the maximum uncertainty along the path, while the time constraints were always verified. The results of this analysis is reported in Table I. It is evident that the proposed solution, which is solely based on local information and is applied as a reactive control, can be well compared with the optimal path using global information.

V. Experimental Results

In this section the validity of the proposed APF-based approach has been confirmed with several experiments on the field in a 6×6 m^2 arena equipped with 14 OptiTrack calibrated cameras ensuring positioning accuracy in the oder of a few mm. Also, the mobile robot and the testing area have been instrumented with DecaWave UWB transceivers for ranging measurements (see Figure 12). The adopted DWM1001 module is based on the well-known DWM1000 UWB transceiver, which includes a DWM1000 UWB transceiver (compliant with the IEEE802.15.4 UWB physical layer), a Nordic Semiconductor nRF52832 micro-controller unit (MCU) with Bluetooth Low Energy (BLE) support, and a 3-axis accelerometer. Such devices rely on an IEEE 802.15.4a standard technique with Two-Way-Ranging-Time-Of-Arrival (TWR-TOA) for accurate localisation. To prevent interference, only two TWR-TOA communications can be active simultaneously.

As to the experiments, we considered different initial and final target positions (s_i and s_e) as well as different deployments of the anchors. In the symmetric case (see Figure 13-a), $s_i = [1.2, 2.2]$ [m] and two target destination points, i.e., $s_e = [1.5, -1]$ [m] (target 1) and $s_e = [-1.5, -1]$ [m]

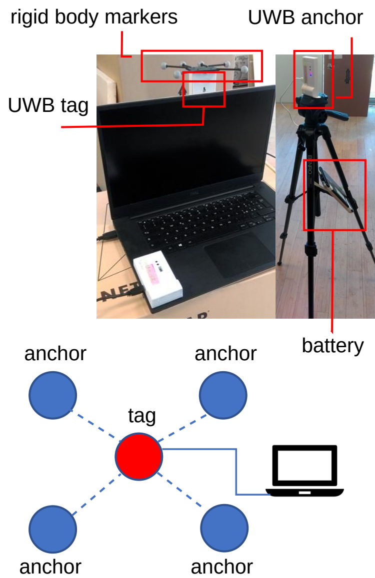

Fig. 12. Experimental setup based on the DecaWave MDEK UWB positioning system.

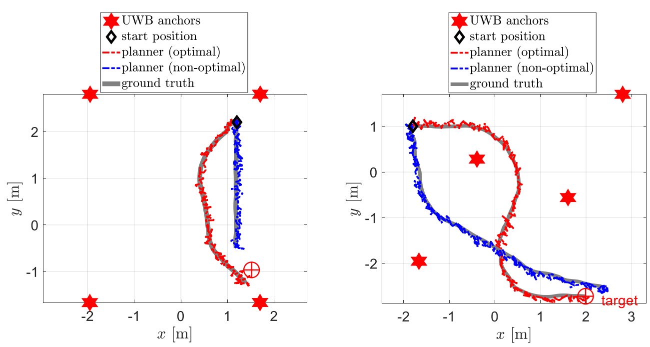

(a) (b)

Fig. 13. Optimal (red) and non-optimal (blue) trajectories taken by the robot in (a) symmetric and (b) asymmetric deployments of the anchors to reach the target 1 and target 3, respectively.

(target 2), are considered. Instead, for the asymmetric anchors deployment (see Figure 13-b), we have the starting position $s_i = [-1.8, 1]$ [m], while the target 3 destination point is $s_e = [2, -2.8]$ [m].

The tag mounted on the robot (see Figure 14-a) communicates with each anchor within a 25 ms time interval. The experiments are conducted in an environment where some of the simplifying assumptions underlying the APF-based approach (e.g., the Gaussian distribution of the sensor uncertainty contributions) are no longer true. Indeed, Figure 15-a reports the box-and-whiskers plot of the ranging measurement errors for each one of the four anchors installed, assuming that the OptiTrack uncertainty is negligible. Clearly, the distance measurement data from the anchors are biased. The Time-Division Multiple Access (TDMA) scheme implemented in the real devices to exchange the UWB messages causes an

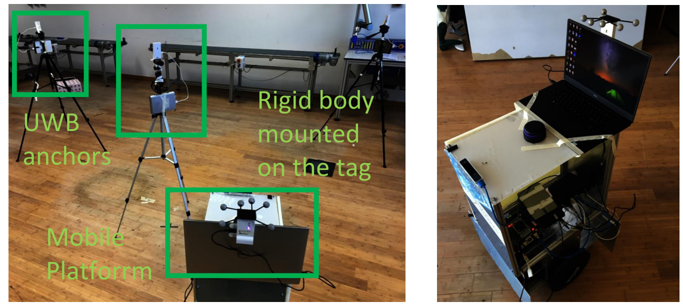

(a) (b)

Fig. 14. (a) Partial view of the experimental arena and (b) a snapshot of the testing robot.

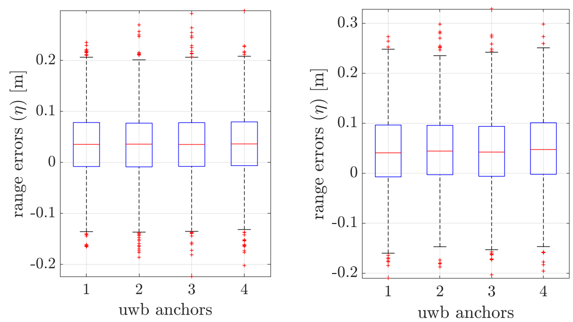

(a) (b)

Fig. 15. UWB ranging errors sampled while the robot is moving with (a) $v_k = 0.4$ [m/s] and (b) $v_k = 0.8$ [m/s].

additional source of uncertainties which was not considered in the simulations, i.e. the latency of measurement data. The effect of latency becomes more prominent when the robot moves with a higher forward velocity. In fact, the distance measurement errors are larger and more visible in Figure 15-b (when the robot moves at $v_k = 0.8$ m/s) compared to the case when $v_k = 0.4$ m/s (see Figure 15-a).

Relying on the sample variances of the raw experimental sensor data, first we found that $\sigma_{\tilde{z}_i} = 67$ mm, for $i = 1, \ldots, 4$, $\sigma_v = 0.09$ m/s and $\sigma_\omega = 0.06$ rad/s, and then we planned 3 different paths computed with the TM method for the chosen three target destination points. Such paths are labelled as "optimal" in Figure 13) after setting the forward velocity v_k of the robot to 0.4 m/s. For comparison, we have also generated 3 additional sample paths that minimise the travel time to the target (denoted as "non-optimal" in Figure 13). Moreover, to account for the effect of the TDMA latency, dual experiments with the robot velocity $v_k = 0.8$ m/s were conducted. While Figure 13 offers just a qualitative comparison of the two results, in which it is clearly visible that the non-optimal trajectory does not reach correctly the target, the quantitative comparison is reported in Table II, where the RMS position errors are shown. Despite the challenging experimental scenario, the positioning uncertainty is clearly smaller even if the path is clearly longer (see Figure 13).

	v_k [m/s]	Target	Anchors deployment	RMSE$_{x,y}$
optimal	0.4	1	symmetric	0.042
	0.4	2	symmetric	0.039
	0.4	3	asymmetric	0.048
	0.8	1	symmetric	0.054
	0.8	2	symmetric	0.050
	0.8	3	asymmetric	0.064
non-optimal	0.4	1	symmetric	0.051
	0.4	2	symmetric	0.048
	0.4	3	asymmetric	0.058
	0.8	1	symmetric	0.055
	0.8	2	symmetric	0.063
	0.8	3	asymmetric	0.074

TABLE II. EXPERIMENTAL RMS POSITION ERRORS FOR THE OPTIMAL AND NON-OPTIMAL PATHS FOLLOWED BY THE ROBOT WHEN IT MOVES AT TWO DIFFERENT FORWARD VELOCITIES.

VI. CONCLUSIONS

We have shown an uncertainty-drive path planning strategy for mobile robots able to ensure a good tradeoff between a steady progress towards the goal and the localisation uncertainty on the way. The potential field-like approach synthesises a path that limits the uncertainty growth by using the closed-form expressions of the covariance matrix of the state estimation errors. Fine tuning of the parameters of the proposed approach and optimality of the solutions are confirmed through Monte Carlo simulations. Experimental evidence shows that the proposed solution yields a lower standard positioning uncertainty than other more common path planning algorithms (e.g., conceived to minimise the time to reach the target).

Several problems remain open for future research. Three of them are worth mentioning: i) replacing our two steps control strategy (i.e., estimating the gradient using the uncertainty on the Cartesian components and then estimating the step size using angular uncertainty) with a one step solution in which Cartesian and angular uncertainties are considered at the same time; ii) applying the same ideas to reduce the uncertainty affecting the position of the anchors (i.e., the mapping problem); iii) extending the application of these ideas to a broader class of systems (e.g., car-like robots, unicycle robots with trailers, quadrotors and so on).

REFERENCES

[1] F. Shamsfakhr, L. Palopoli, D. Macii, and D. Fontanelli, "Ruling uncertainties in Range-only Robot Localisation," in *Proc. IEEE Int. Instrumentation and Measurement Technology Conference (I2MTC)*. Glasgow, Scotland: IEEE, May 2021, pp. 1–6.

[2] P. Chen, Y. B. Xu, L. Chen, and Z. A. Deng, "Survey of WLAN fingerprinting positioning system," *Applied Mechanics and Materials*, vol. 380, pp. 2499–2505, Aug. 2013.

[3] A. Motroni, P. Nepa, V. Magnago, A. Buffi, B. Tellini, D. Fontanelli, and D. Macii, "SAR-based Indoor Localization of UHF-RFID Tags via Mobile Robot," in *International Conference on Indoor Positioning and Indoor Navigation (IPIN)*. Nantes, France: IEEE, Sept. 2018, pp. 1–8.

[4] P. Nazemzadeh, F. Moro, D. Fontanelli, D. Macii, and L. Palopoli, "Indoor Positioning of a Robotic Walking Assistant for Large Public Environments," *IEEE Trans. on Instrumentation and Measurement*, vol. 64, no. 11, pp. 2965–2976, Nov 2015.

[5] B. Dzodzo, L. Han, X. Chen, H. Qian, and Y. Xu, "Realtime 2D code based localization for indoor robot navigation," in *Proc. IEEE Int. Conference on Robotics and Biomimetics (ROBIO)*, Shenzhen, China, Dec. 2013, pp. 486–492.

[6] V. Magnago, L. Palopoli, A. Buffi, B. Tellini, A. Motroni, P. Nepa, D. Macii, and D. Fontanelli, "Ranging-free UHF-RFID Robot Positioning through Phase Measurements of Passive Tags," *IEEE Trans. on Instrumentation and Measurement*, vol. 69, no. 5, pp. 2408–2418, May 2020.

[7] P. Nazemzadeh, D. Fontanelli, D. Macii, and L. Palopoli, "Indoor Localization of Mobile Robots through QR Code Detection and Dead Reckoning Data Fusion," *IEEE/ASME Transactions on Mechatronics*, vol. 22, no. 6, pp. 2588–2599, Dec. 2017.

[8] M. J. Gallant and J. A. Marshall, "Two-dimensional axis mapping using LiDAR," *IEEE Trans. on Robotics*, vol. 32, no. 1, pp. 150–160, Feb. 2016.

[9] Y. Zhou, Jun Li, and L. Lamont, "Multilateration localization in the presence of anchor location uncertainties," in *2012 IEEE Global Communications Conferenc (GLOBECOM)*, 2012, pp. 309–314.

[10] D. Macii, A. Colombo, P. Pivato, and D. Fontanelli, "A Data Fusion Technique for Wireless Ranging Performance Improvement," *IEEE Trans. on Instrumentation and Measurement*, vol. 62, no. 1, pp. 27–37, Jan. 2013.

[11] D. Giovanelli, E. Farella, D. Fontanelli, and D. Macii, "Bluetooth-based Indoor Positioning through ToF and RSSI Data Fusion," in *International Conference on Indoor Positioning and Indoor Navigation (IPIN)*. Nantes, France: IEEE, Sept. 2018, pp. 1–8.

[12] K. Cheok, M. Radovnikovich, P. Vempaty, G. Hudas, J. Overholt, and P. Fleck, "UWB tracking of mobile robots," in *Proc. IEEE International Symposium on Personal Indoor and Mobile Radio Communications (PIMRC)*, Instambul, Turkey, Sep. 2010, pp. 2615–2620.

[13] DecaWave, "DW1000 Data Sheet," 2016.

[14] G. P. Huang, N. Trawny, A. I. Mourikis, and S. I. Roumeliotis, "Observability-based consistent ekf estimators for multi-robot cooperative localization," *Autonomous Robots*, vol. 30, no. 1, pp. 99–122, 2011.

[15] G. L. Mariottini, G. Pappas, D. Prattichizzo, and K. Daniilidis, "Vision-based localization of leader-follower formations," in *Proceedings of the 44th IEEE Conference on Decision and Control*. IEEE, 2005, pp. 635–640.

[16] S. Cedervall and X. Hu, "Nonlinear observers for unicycle robots with range sensors," *IEEE transactions on automatic control*, vol. 52, no. 7, pp. 1325–1329, 2007.

[17] L. Palopoli and D. Fontanelli, "Global Observability Analysis of a Nonholonomic Robot using Range Sensors," in *European Control Conference (ECC)*, San Petersburg, Russia, May 2020.

[18] V. Magnago, P. Corbalán, G. Picco, L. Palopoli, and D. Fontanelli, "Robot Localization via Odometry-assisted Ultra-wideband Ranging with Stochastic Guarantees," in *Proc. IEEE/RSJ International Conference on Intelligent Robots and System (IROS)*. Macao, China: IEEE, Oct. 2019, pp. 1–7, accepted.

[19] D. Fontanelli, F. Shamsfakhr, D. Macii, and L. Palopoli, "An Uncertainty-driven and Observability-based State Estimator for Nonholonomic Robots," *IEEE Trans. on Instrumentation and Measurement*, vol. 70, pp. 1–12, 2021, available on line.

[20] P. Salaris, M. Cognetti, R. Spica, and P. R. Giordano, "Online optimal perception-aware trajectory generation," *IEEE Transactions on Robotics*, vol. 35, no. 6, pp. 1307–1322, 2019.

[21] C. W. Warren, "Global path planning using artificial potential fields," in *1989 IEEE International Conference on Robotics and Automation*. IEEE Computer Society, 1989, pp. 316–317.

[22] R. Zekavat and R. M. Buehrer, *Handbook of position location: Theory, practice and advances*. John Wiley & Sons, 2011, vol. 27.